ACS OMEGA

Open Access

http://pubs.acs.org/journal/acsodf

Article

In Situ Liquid Cell Transmission Electron Microscopy Study of Studtite Particle Formation and Growth via Electron Beam Radiolysis

Nick Kurtyka, Brian van Devener, Brandon W. Chung, and Luther W. McDonald, IV*

Cite This: *ACS Omega* 2023, 8, 48336−48343

Read Online

ACCESS | Metrics & More | Article Recommendations | Supporting Information

ABSTRACT: This study presents in situ observations of studtite ($UO_2O_2(H_2O)_2 \cdot 2H_2O$) crystal growth utilizing liquid phase transmission electron microscopy (LP-TEM). Studtite was precipitated from a uranyl nitrate hexahydrate solution using hydrogen peroxide formed by the radiolysis of water in the TEM electron beam. The hydrogen peroxide (H_2O_2) concentration, directly controlled by the electron beam current, was varied to create local environments of low and high concentrations to compare the impact of the supersaturation ratio on the nucleation and growth mechanisms of studtite particles. The subsequent growth mechanisms were observed in real time by TEM and scanning TEM imaging. After the initial precipitation reaction, a post-mortem TEM analysis was performed on the samples to obtain high-resolution TEM images and selected area electron diffraction patterns to investigate crystallinity as well as energy-dispersive X-ray spectroscopy spectra to ensure that studtite was produced. The results reveal that studtite particles form through various mechanisms based on the concentration ratio of uranyl to H_2O_2 and that studtite is initially produced through an amorphous intermediary prior to formation of the crystalline material commonly reported in the literature.

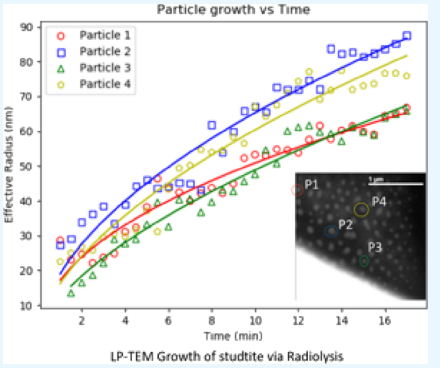

INTRODUCTION

Controlling particle morphology is of great importance to many industries including semiconductors, nanomaterials, and steel fabrication.[1−4] Levlev et al. showed that a mechanistic understanding of nucleation and growth mechanisms can lead to improved modeling of material properties and future material discovery.[5] In the nuclear industry, particle morphology can impact the environmental transport of uranium, nuclear fuel performance in reactors, long-term storage of spent nuclear fuel, and support nuclear forensics and nuclear safeguards in identifying the processing history of nuclear materials.[4,6,7] Prior studies have identified many variables including pH, temperature, reaction time, and calcination temperature that impact the final particle morphology.[6−10] Advancements in particle segmentation and machine learning enable quantification of even subtle morphology changes.[11,12] The challenge, however, has been in understanding the fundamental principles that result in unique particle morphologies based on the chemical and physical processing conditions. In situ liquid phase transmission electron microscopy can help reveal the underlying mechanisms of particle formation, particularly when the impacts of radiolysis can be mitigated.[13,14] In the case of studtite, electron beam radiolysis of uranyl solutions enables the controlled in situ precipitation of particles under different reaction conditions.

Studtite is a highly important uranyl precipitate that is routinely made in uranium mining and nuclear fuel processing. It is even considered to be one of the primarily degradation pathways of UO_2 fuel exposed to moisture in a long-term waste repository.[15,16] Commercially, studtite is prepared by adding hydrogen peroxide to uranyl solutions.[17,18] In waste, radiolysis of water results in the formation of hydrogen peroxide and subsequent formation of studtite.[7,19,20] The morphology of the studtite has a major impact on a nuclear fuel's performance and the migration rates of uranium in the environment.[21] Unfortunately, mechanisms explaining how studtite particles are formed is missing. Previously, Buck et al. performed in situ liquid cell scanning electron microscopy experiments to radiolytically produce studtite.[22] They started from an initial solution of ammonium uranyl carbonate, performed extensive modeling of the electron beam radiolysis, and used bromide solutions to control the amount of H_2O_2 produced.[22] Using in situ liquid phase transmission electron microscopy (LP-TEM), we aim to expand this early work to probe studtite particle formation mechanisms.

Previously, in situ LP-TEM has been used to study complex nonclassical growth mechanisms. LP-TEM allows for the high

Received: October 5, 2023
Revised: November 10, 2023
Accepted: November 15, 2023
Published: December 5, 2023

spatial resolution imaging of bulk nucleated particles observed with a standard with electron microscopy while also having the temporal resolution to capture the early stages of crystallization pathways that are too fast for similar in situ techniques, like scanning probe microscopy[14] Obtaining direct evidence of complex crystallization mechanisms in real time has significantly advanced with the development of more intricate liquid cell designs that accommodate various nucleation and growth event triggers.[14]

In the case of precipitating studtite ($UO_2O_2(H_2O)_2{\cdot}2H_2O$), there are two methods to trigger precipitation events. In the most traditional LP-TEM setup, a liquid flow cell would be used to mix a solution of UNH and hydrogen peroxide in the viewing area. However, this poses a number of experimental challenges due to the high-energy electrons used to image the system. The electron beam will irradiate the aqueous solution forming radiolytic species including e_{aq}^-, $H^{\cdot}$, $OH^{\cdot}$, H_2, H_2O_2, H^+, and OH^-.[23] With hydrogen peroxide also produced through radiolysis, it would be very challenging to discern which precipitated studtite particles were formed from the hydrogen peroxide provided by the precursor solution or were produced via radiolysis.

To overcome these limitations, the second LP-TEM method foregoes the use of a flow cell, instead using a static cell relying solely on the electron beam to produce the hydrogen peroxide needed for studtite precipitation. By using a static cell, the preparation and execution of the precipitation are simplified and it allows the local hydrogen peroxide concentration to be directly controlled by the electron beam.[24] Using this method, we performed the first in situ LP-TEM precipitation of studtite. The local hydrogen peroxide concentration was controlled using the current of the TEM beam and then varied to determine the effect that it has on the overall studtite growth mechanism. It is then demonstrated that under the experimental conditions, studtite does not nucleate and grow in a classical crystalline fashion. Instead, it goes through an amorphous precursor phase before inevitably crystallizing when dried.

EXPERIMENTAL SECTION

Preparation of Starting Chemicals. One gram of A-UO_3 was dissolved in 30 mL of 8 M nitric acid and subsequently boiled off at 95 °C three times for approximately 24 h. The resulting uranyl nitrate crystals were dissolved in 18 MΩcm water and diluted to form a 1 M UNH solution. Studtite was then synthesized by titrating (1 mL/min) a total of 30 mol % excess of 30 wt % H_2O_2. The solution was allowed to react for 30 min. The studtite was then vacuum filtrated with five 40 mL 18 MΩcm water washes. After a 24 h drying period in a room temperature vacuum storage chamber, the studtite was calcined to A-UO_3 at 400 °C for 8 h under a 500 mL/min flowing N_2 atmosphere. The first precipitation and subsequent calcination were done to ensure the purity of the starting solution.[25] Uranyl nitrate was then synthesized again by the same hydrothermal process described above. Last, a balance of 18 MΩcm water was used to make the 10 mM UNH solution (pH 2) used in the in situ experiment.

In Situ TEM Analysis. TEM analysis was done using a JEOL JEM 2800 Scanning Transmission Electron Microscope in the Electron Microscopy and Surface Analysis Lab at the University of Utah. A Poseidon Select: TEM Liquid Microscopy Cell with a corresponding silicon nitride (SiN) static liquid cell E-chip set consisting of a 550 × 50 μm window bottom chip and a 4 × 8 array of 20 × 20 × 0.17 μm well microwell top chip (Protochips Inc., Morrisville, NC) was used. The electron transparent SiN viewing windows are 30 nm-thick. The real-time imaging was acquired with a Gatan Microscopy Suite/Gatan Micrograph (Gatan Ametek, Pleasanton, CA) and recorded using Open Broadcaster Software (OBS) Studio (developed by OBS Studio Contributors). The videos were then imported to VLC Media Player (developed by VideoLAN project) and ImageJ (National Institutes of Health), which were used for video and particle analysis, respectively. The SAED patterns were analyzed using both Gatan Micrograph and Single Crystal (CrystalMaker Software Limited, Oxfordshire, UK).

To prepare the E-chips for the experiments, the photoresist was removed and the chip was washed in an acetone bath for 10 min followed by an ethanol bath for 10 min. The E-chips were subsequently dried using compressed air, plasma cleaned, and finally loaded into the Poseidon Select in situ holder with a 1 μl aliquot of the 10 mM UNH starting solution. Promptly, the vacuum seal was fully assembled and the chamber was inspected for leaks and cracks in the chamber. After the leak check, a final plasma cleaning of the reaction chamber was done before it was placed into the TEM column.

The TEM was operated at 200 keV with a 1 nm probe and 1 nA probe current. The STEM settings were a 1.2 μs dwell time with a 1024 × 1024 pixel area leading to approximately 1.7191 s per frame as reported by Gatan Micrograph software. After the in situ precipitation experiment, the microchips were kept and dried in a room temperature vacuum storage chamber. Post-mortem analysis was performed to obtain selected area electron (SAED), energy-dispersive X-ray spectroscopy (EDS/EDX), and HRTEM data.

Concentration and Dose Rate Calculations. A kinetic model developed by Schneider et al. was used to estimate the H_2O_2 concentration produced by radiolysis. The necessary parameters were the starting solution chemistry, *G*-values for the given radiation type and energy, and approximate dose rate. More details on the model as well as access to the model script are available in ref 24. To calculate the dose rate for a thin liquid layer in TEM mode, the following equation from Schneider et al.'s work was used:

$$D = \frac{\frac{dE}{dx}\cdot 10^5 I}{\pi a^2}$$

where D is the dose rate (Gy/s), dE/dx is the density-normalized stopping power of an electron in water, a is the beam radius, 10^5 is a conversion factor, and I is the probe current. However, the equation must be adapted to consider STEM imaging.

$$D = \frac{\frac{dE}{dx}\cdot 10^5 I_p}{A}$$

Instead of the beam radius, the total image area or STEM scan area (A) is used to avoid beam broadening issues and sampling errors due to magnification changes.[23,26] The probe current is changed to approximated probe current I_p. The approximated probe current is calculated by multiplying the probe current by a ratio of 1 s to the frame time τ. The approximated probe current was used to account for the fact that STEM imaging has a lower temporal resolution than TEM imaging.[13,23]

https://doi.org/10.1021/acsomega.3c07743
ACS Omega 2023, 8, 48336−48343

The STEM videos produced in this study had a total scan time of 1.719 s per frame, which means that over the course of 1 s, the beam has deposited electrons equivalent to the probe current but only in a small portion of the viewing area. This creates an inconsistency in the dose rate calculation for the kinetic model because only 58% of the viewing area has had direct interaction with the beam, while 42% of the viewing area has only been exposed to diffused electrons and radiolysis products. Using the approximated probe current, however, provides an estimate of the effective current received by the entire viewing area during a portion of the STEM scan, which will better represent the H_2O_2 concentration calculated by the kinetic model. To calculate the dose rate per frame seen in the STEM sequences, the beam current is multiplied by the frame time and divided by the total scan area and the elemental charge constant: $(I{\cdot}\tau)/(C{\cdot}A)$.[23] The dose rates for the TEM images were calculated in a similar fashion by replacing the frame time with exposure time.

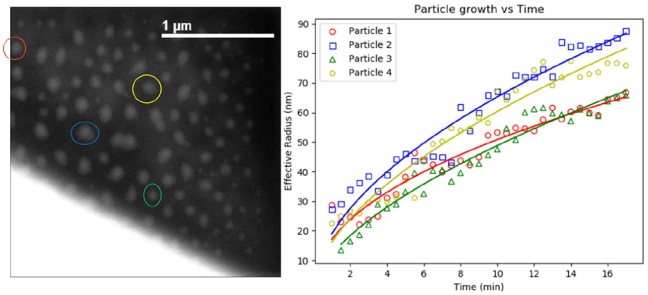

Figure 1. Plot of the effective radius of the four circled particles from sequence 1 over the course of 17 min.

RESULTS AND DISCUSSION

Precipitate Formation through Radiolysis. Studtite was precipitated under three electron dose rates to vary the ratio of hydrogen peroxide to uranyl. In the first STEM image sequence, a low H_2O_2 concentration of approximately 3 mM was achieved using an electron dose rate of ~20.1 $e^-/(Å^2\ f)$ (Figure 2). It is important to note that these are estimates of the hydrogen peroxide concentration; many other radicals will be formed during radiolysis. Buck et al. summarized all radiolysis species, and our H_2O_2 concentration is similar to their modeling estimates.[22] In their 15 keV beam at 0.25 Gy/s, they estimated approximately 3 μM of H_2O_2 to be produced at the steady state. In this study, we estimate 3 mM H_2O_2 for a 200 keV beam at 3.1 × 10^7 Gy/s at the steady state.

The first signs of visible particle formation occur after 30 s of constant irradiation with a large number of seemingly low-density spherical particles. Due to the relatively simple and stable growth of the particles, it was possible to quantitatively analyze the mechanisms involved by measuring the effective radius of four random particles at 30 s intervals for a duration of 17 min (Figure 1).

The effective radius growth was fitted with a power law model using the SciPy library in Python. The resulting fitted curves show the $r_{eff} \propto t^{1/2}$. By assuming the Lifshitz−Slyozov−Wagner (LSW) kinetic model under these precipitation conditions, a $t^{1/2}$ growth rate suggests that the growth mechanism is reaction-limited.[27−29] This is consistent with the reactant concentration ratio of uranyl nitrate to H_2O_2 being ~3.3:1.

The second STEM sequence was initially taken at the same magnification (e.g., dose rate) as Video 1 (Figure 3). However, the nucleation of particles against the surface of the SiN well began almost immediately, which is representative of heterogeneous nucleation. The solid well wall provides a stable nucleating surface, effectively reducing the energy needed to precipitate out of solution.[14,30,31] The homogeneous nucleation took slightly longer compared to the particles nucleated on the wall with the first signs of precipitation occurring at 19 s. At 30 s, the magnification was increased, resulting in an electron dose rate of approximately 87.5 $e^-/(Å^2\ f)$ and a H_2O_2 concentration of ~5.6 mM. During this increase in magnification, there was no noticeable change in growth mechanisms as compared to sequence 1.

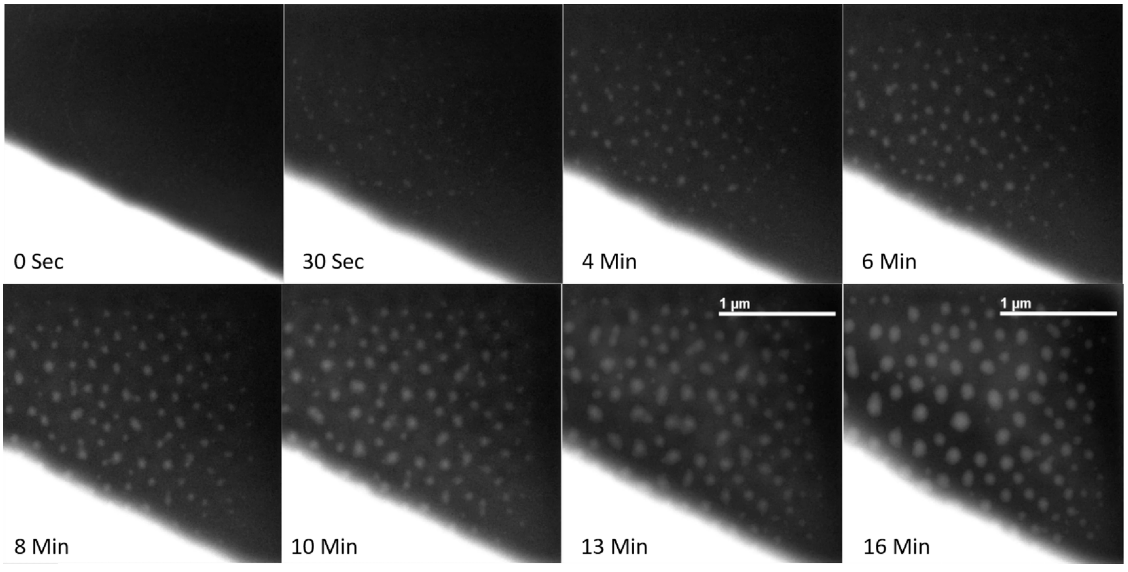

Figure 2. Time sequence of STEM images depicting the growth of studtite with an approximate electron dose rate of 20.1 $e^-/(Å^2\ f)$ corresponding to a H_2O_2 concentration of 3 mM.

https://doi.org/10.1021/acsomega.3c07743
ACS Omega 2023, 8, 48336−48343

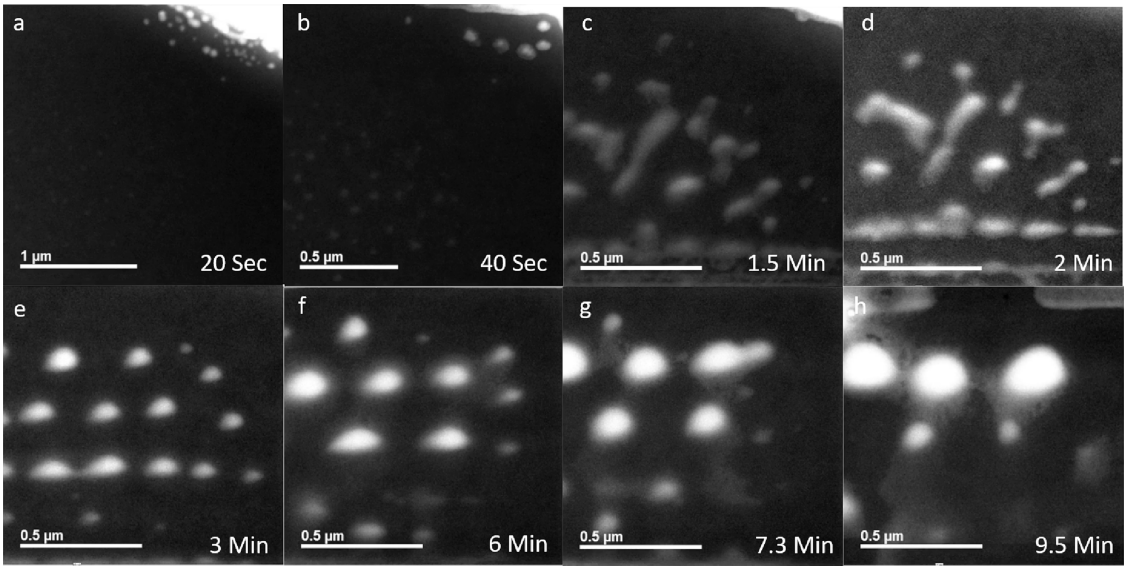

Figure 3. (a–h) Second time sequence of STEM images at variable electron dose rates (~20.1–124 $e^-/(Å^2\ f)$) resulting in local H_2O_2 concentrations between 3 and 6.5 mM.

At 45 s, the magnification was increased again corresponding to an electron dose rate of ~124 $e^-/(Å^2\ f)$ and a H_2O_2 concentration of 6.5 mM. The higher magnification was held for 17 s, and during this time, the growth of the particles changed drastically. Instead of small spherical particles similarly seen in the first sequence, the particles were thin and elongated, promoting aggregation between particles nearby and forming nondistinctive low-density masses. Then, as seen in Figure 3d, small, high-density nuclei form within the elongated low-density masses. Under these conditions, it is reasonable to assume that the low-density masses provided a stabilizing environment to facilitate the formation of higher-density particles.

Similar behavior has been observed in the calcium carbonate system.[32,33] Nielson et al. showed that calcium carbonate, a naturally occurring mineral, has unique crystallization pathways that can rely on a bulk amorphous precursor.[32] The amorphous phase is thermodynamically metastable; however, the free energy barrier is smaller than the stable more crystalline phase, allowing it to form first.[31,34] The amorphous phase then acts as a secondary nucleation site, lowering the nucleation energy barrier of the stable phase. The amorphous precursor pathway is commonly referred to as the Ostwald step rule.[34,35] Another similar phenomenon has been seen in gold nanoparticle formation and protein nucleation, suggesting that the precipitation event may be described by a two-step mechanism.[34,36−39] The two-step mechanism assumes that the nucleation is split into an initial formation of a "dense droplet" solute-enriched secondary liquid phase followed by the crystallization taking place within the enriched phase.[37,38] The liquid phase forms due to a liquid–liquid spinodal decomposition or, similar to the Ostwald step rule pathway, a metastable liquid embryo is kinetically more favorable. When showing that gold nanoparticles may follow the two-step method via in situ atomic force microscopy (AFM) imaging, Mikhlin et al. suggested that the interactions between the system, the HOPG support, and the cantilever can indicate the phase. The HOPG flattened the products, and the cantilever would easily stretch them, which may indicate a liquid droplet or at least a soft matter.[36] However, an AFM study is difficult due to the time-intensive nature of AFM combined with the relatively short life of the precipitated phase. Therefore, more experimental methods must be explored to verify these hypotheses in the studtite system.

After formation of high-density nuclei, the particles began to coarsen and shrink, reverting back to oblong oval-shaped dense particles (Figure 3e). The newly condensed particles grew primarily through agglomeration and Ostwald ripening. Figure 3f shows the beginning of the formation of shells, surrounding the condensed particles, of newly precipitated solutes, creating an expansive interconnected network between the larger denser particles. In Figure3g,h the web-like network seemed to facilitate the agglomeration and Ostwald ripening, resulting in a significant reduction in the number of particles with most being dissolved into three main particles after 6.5 min. This behavior may again be indicative of the two-step mechanism with similar globule shells forming around the condensed solute clusters. It has been suggested that these globules form in part due to the stability of the anion complexes as well as the low local activities of molecular species involved in the reactions.[36,39] Relating it back to the studtite precipitation, the 17 s increased magnification and subsequent reduction in magnification spurred the formation of larger particles and reduced the activity of H_2O_2, resulting in a lower concentration of studtite monomers. This created an environment where the globule shell can form.

The third STEM sequence (Figure S2 and SI Video 3) was initially imaged with a STEM electron dose rate of approximately 87.5 $e^-/(Å^2\ f)$, similar to the majority of the second video. The nucleation and growth were similar to the process seen in the first sequence where there was an initial mass nucleation followed by growth primarily through solute diffusion with some agglomeration. However, due to window dewetting, quantitative particle growth measurements could not be obtained. To avoid losing the recorded region, it was necessary to zoom out and reset the image.

With the image reset, magnification was increased corresponding to an electron dose of approximately 224 $e^-/(Å^2\ f)$, resulting in a H_2O_2 concentration of ~8.2 mM. Thus, the H_2O_2 is almost equimolar in the system with a ratio of

https://doi.org/10.1021/acsomega.3c07743
ACS Omega 2023, 8, 48336−48343

uranyl to H_2O_2 of 1.21:1. Similar to the growth event in sequence 2, the precipitated particles thinned and elongated, forming the low-density masses that quickly condense into the stabilized dense oblong particles. After about 1.5 min, there was a burst of nucleations and growth of these interconnected elongated chains that eventually swallowed the dense particles and covered the entire imaged region. This may be evidence of a direct crystallization pathway. Similar to calcium carbonate which has been observed to follow both the Ostwald step mechanism crystallizing indirectly through an amorphous phase and also crystallizing directly during precipitation.[32,34] The higher supersaturation due to the magnification in combination with a high local uranyl ion concentration may have facilitated large-scale immediate precipitation that bypassed any precursor phase.

TEM Imaging of Precipitates. To verify the formation of studtite in the STEM videos above, an in situ experiment was performed again but using only TEM imaging to obtain SAED data and help identify the composition of the crystalline phases. As seen in the SAED patterns (Figure 4), all of the particles are primarily amorphous with small amounts of varying crystallinity. These results do not conclusively show that studtite is formed, but combined with the post-mortem results, it does show that studtite can form through an amorphous phase/precursor phase before eventually crystallizing into the known studtite most commonly reported in the literature.[42] Based on the chemical species present, particularly uranyl nitrate hexahydrate and hydrogen peroxide, it is reasonable to assume the precipitated phases are most likely studtite.[22] Furthermore, it is obvious that STEM and TEM imaging modes have differing effects on the growth of the particles. Figure 1 again shows how the precipitated particles grow during STEM imaging at an approximate H_2O_2 concentration of 3 mM. Figures 4 and 5 show the particle growth during TEM imaging at a maximum approximate H_2O_2 concentration of ~3.9 mM. According to sequences 2 and 3, a similar growth mechanism to sequence 1 should be seen up until ~6.5 mM. However, the TEM imaging caused the particles to reshape and expand into amorphous masses that lack the defined boundaries seen in sequences 2 and 3.

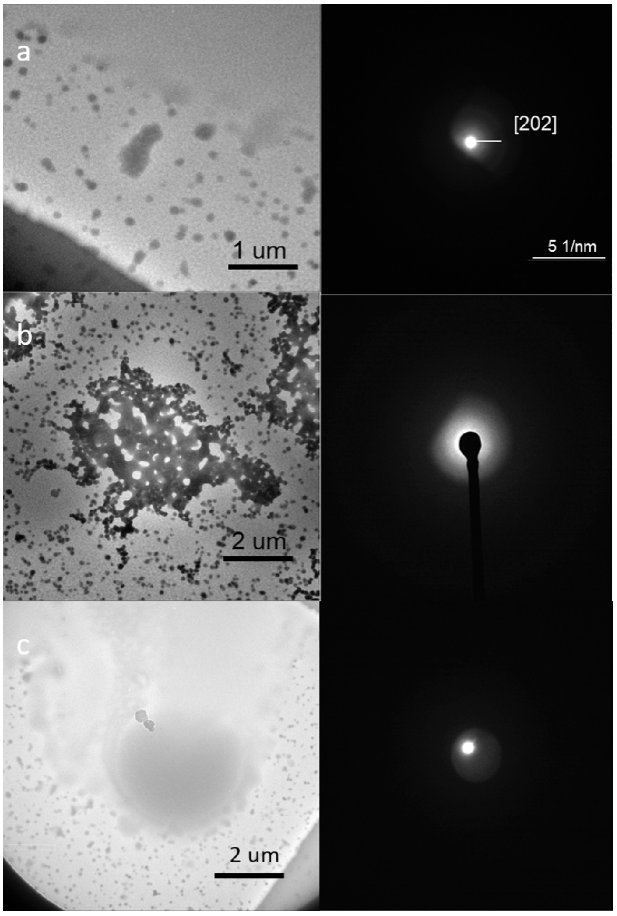

Figure 4. (a–c) TEM images with their corresponding SAED patterns showing the initial amorphous studtite forms before eventually crystallizing.

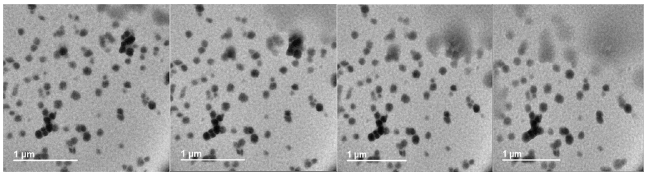

Figure 5. TEM mode captured sequence showing the amorphizing nature of the electron beam over the course of 30 s.

Solid studtite has been reported to completely amorphize under a 200 keV TEM beam at a dose rate between ~5.1 and 15.4 $e^-/Å^2$ and partially amorphize beginning at 0.5 $e^-/Å^2$.[40] The dose rate seen in Figure 5 is ~4.93 $e^-/Å^2$ f and increases only when taking the diffraction pattern. There is no clear reason behind the difference in amorphizing seen in the STEM and TEM images.

Typically, imaging in TEM mode will result in a higher cumulative dose due to the higher exposure time.[23] However, because the same current was used in both imaging modes, the cumulative dose was similar enough not to justifiably explain the difference. For example, the electron dose per angstrom squared over a 30 s time interval in sequence 1, which has the lowest magnification and lowest dose, was 351 $e^-/Å^2$, while in Figure 5, it was 296 $e^-/Å^2$. It is possible that the increased amorphization in TEM mode arises because of its nonlocal parallel beam. The TEM beam provides constant direct irradiation to precipitates, while the STEM beam only directly irradiates a particle for a few microseconds every 1.7 s. This disparity in direct irradiation time could result in more specimen damage and inevitably the drastic precipitate evolution seen during imaging in TEM mode.

It has been shown that the inelastic scattering producing radiolysis effects will change the structure and potentially remove mass from a solid specimen.[43] The radiolysis effect on the precipitate is especially prevalent because studtite's structure contains a significant amount of oxygen species. For example, crystalline SiO_2 radiolysis is known to create amorphous specimen through Frenkel-type defects, creating peroxy species and oxygen vacancies with continuous irradiation causing complete order loss.[44,45] The beam electrons will excite an oxygen bond resulting in configurational instability, allowing the oxygen to move and complex with nearby neighbors.[46] In terms of studtite, this can manifest with the uranyl oxygens complexing with peroxy oxygens, nearby waters bonded to the uranium core, ionized oxygens being attacked by protons in the acidic solution, or peroxy bonds being split. The split peroxy oxygens will also increase

https://doi.org/10.1021/acsomega.3c07743
ACS Omega 2023, 8, 48336−48343

the oxygen gas production, which was a constant issue during imaging in TEM mode. Initial bubble formation can be seen in Figure 4c. All of these radiolysis degradation effects reduce the stability of the studtite, letting it easily be redissolved into the acidic solution. The newly dissolved studtite can then be immediately reprecipitated out of solution due to the consistent hydrogen peroxide concentration produced from constant beam irradiation. This may explain the rapid expansion of the particles under the TEM beam.

Despite the discrepancy between imaging modes, it is evident from the SAED patterns collected that studtite will initially precipitate in an amorphous phase within solution. Images shown in Figure 4a,b were formed outside of the viewing window via the diffusion of imparted electrons and radiolysis products. Their formation shows that without a direct electron beam interaction facilitating particle amorphization, UNH and H_2O_2 will still precipitate an amorphous studtite phase. The significant production of solid uranyl oxide phases outside the irradiated area is in agreement with the results that Buck et al. reported during a similar experiment implementing lc-SEM.[22,47]

Post-mortem Analysis of Precipitates. According to both the Ostwald step and two-step mechanisms, the amorphous phase and dense liquid droplets are stable or metastable precursors for the crystalline phase.[33,34,38] Once the solution is taken out and given time, the free-energy barrier will decrease to a point where the precipitate will favor the conversion to the crystalline phase. Therefore, a post-mortem analysis on the STEM imaged microchips was performed. Most of the dried particles exhibited a kinetically rounded, platelet shape as expected.

The SAED patterns (Figure 6a,b) show that some dried particles kept their amorphous nature, which is in line with

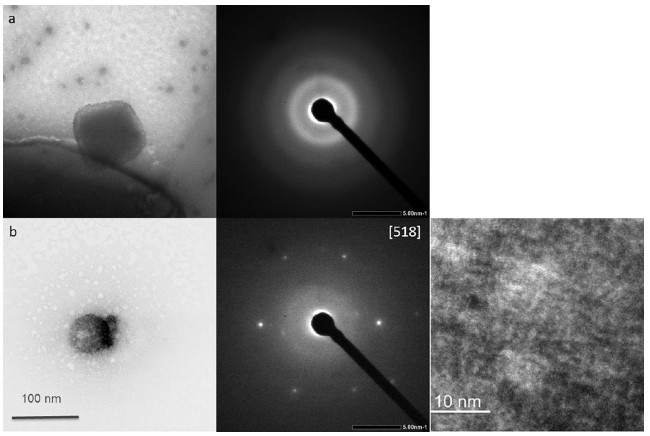

Figure 6. (a, b) Post-mortem high-resolution TEM images and SAED patterns of studtite particles after drying.

being produced through a kinetically dominated reaction.[22] Other particles, however, were almost completely reordered into a single crystal configuration, most likely through post attachment phase transformation.[32,34,41] Through the corresponding SAED pattern and EDS scans, the precipitates were confirmed as studtite with no contaminations.[42]

CONCLUSIONS

In this study, the in situ observation of studtite precipitation via LP-TEM was successfully performed for the first time. It has been shown that depending on the H_2O_2 concentration, various growth mechanisms can occur and that under the experimental conditions, studtite goes through an amorphous precursor phase before eventually crystallizing. At lower concentrations, the system seemed to follow classical mechanisms falling under a reaction-limited regime described by the LSW kinetic model. Once the H_2O_2 concentration reached ~6.5 mM, the growth mechanism drastically changed, forming a secondary low-density phase that stabilized the formation of a high-density core, indicating that to some extent, studtite may follow the two-step mechanism. It was also observed that at almost equimolar reactant concentrations, studtite may also have a direct crystallization pathway similar to its naturally occurring mineral counterpart calcium carbonate.

ASSOCIATED CONTENT

Supporting Information

The Supporting Information is available free of charge at https://pubs.acs.org/doi/10.1021/acsomega.3c07743.

Uranium-based reactions with their corresponding stability constants, third STEM imaging sequence with electron dose rates of 124 and 224 $e^-/(Å^2\ f)$, before and after TEM images with accompanying timelapse SAED patterns, postmortem HRTEM image, SAED pattern, and single crystal overlay and EDS results (PDF)

Videos of the STEM irradiations (MOV, MOV, MOV)

AUTHOR INFORMATION

Corresponding Author

Luther W. McDonald, IV − *Department of Nuclear Engineering, University of Utah, Salt Lake City, Utah 84112, United States;* orcid.org/0000-0001-6735-5410; Email: luther.mcdonald@utah.edu

Authors

Nick Kurtyka − *Department of Nuclear Engineering, University of Utah, Salt Lake City, Utah 84112, United States*

Brian van Devener − *Electron Microscopy and Surface Analysis Laboratory, University of Utah, Salt Lake City, Utah 84112, United States*

Brandon W. Chung − *Lawrence Livermore National Laboratory, Livermore, California 94550, United States;* orcid.org/0000-0002-6395-1239

Complete contact information is available at: https://pubs.acs.org/10.1021/acsomega.3c07743

Author Contributions

The manuscript was written through contributions of all authors. All authors have given approval to the final version of the manuscript.

Funding

This research was supported by the Department of Energy's National Nuclear Security Administration, Office of Defense Nuclear Nonproliferation Research and Development. This work made use of University of Utah USTAR shared facilities supported, in part, by the MRSEC Program of NSF under Award No. DMR-1121252.

Notes

The authors declare no competing financial interest.

■ ACKNOWLEDGMENTS

For B.W.C., this work was performed under the auspices of the U.S. Department of Energy by Lawrence Livermore National Laboratory under Contract DE-AC52-07NA27344. This work made use of Nanofab EMSAL shared facilities of the Micron Technology Foundation Inc. Microscopy Suite sponsored by the John and Marcia Price College of Engineering, Health Sciences Center, Office of the Vice President for Research.

■ REFERENCES

(1) Hsieh, T. H.; Chen, J. Y.; Huang, C. W.; Wu, W. W. Observing Growth of Nanostructured ZnO in Liquid. *Chem. Mater.* **2016**, *28* (12), 4507−4511.

(2) Liu, L.; Sushko, M. L.; Buck, E. C.; Zhang, X.; Kovarik, L.; Shen, Z.; Tao, J.; Nakouzi, E.; Liu, J.; de Yoreo, J. J. Revisiting the Growth Mechanism of Hierarchical Semiconductor Nanostructures: The Role of Secondary Nucleation in Branch Formation. *J. Phys. Chem. Lett.* **2019**, *10* (21), 6827−6834.

(3) Inani, H.; Shin, D. H.; Madsen, J.; Jeong, H. J.; Kwon, M. H.; McEvoy, N.; Susi, T.; Mangler, C.; Lee, S. W.; Mustonen, K.; Kotakoski, J. Step-By-Step Atomic Insights into Structural Reordering from 2D to 3D MoS_2. *Adv. Funct. Mater.* **2021**, *31* (13), 2008395 DOI: 10.1002/adfm.202008395.

(4) Tunes, M. A.; Greaves, G.; Kremmer, T. M.; Vishnyakov, V. M.; Edmondson, P. D.; Donnelly, S. E.; Pogatscher, S.; Schön, C. G. Thermodynamics of an austenitic stainless steel (AISI-348) under in situ TEM heavy ion irradiation. *Acta Mater.* **2019**, *179*, 360−371.

(5) Ievlev, A. v.; Jesse, S.; Cochell, T. J.; Unocic, R. R.; Protopopescu, V. A.; Kalinin, S. v. Quantitative Description of Crystal Nucleation and Growth from in Situ Liquid Scanning Transmission Electron Microscopy. *ACS Nano* **2015**, *9* (12), 11784−11791.

(6) Schwerdt, I. J.; Brenkmann, A.; Martinson, S.; Albrecht, B. D.; Heffernan, S.; Klosterman, M. R.; Kirkham, T.; Tasdizen, T.; McDonald, L. W., IV Nuclear proliferomics: A new field of study to identify signatures of nuclear materials as demonstrated on alpha-UO3. *Talanta* **2018**, *186*, 433−444.

(7) Thompson, N. B. A.; Frankland, V. L.; Bright, J. W. G.; Read, D.; Gilbert, M. R.; Stennett, M. C.; Hyatt, N. C. The thermal decomposition of studtite: analysis of the amorphous phase. *Journal of Radioanalytical and Nuclear Chemistry* **2021**, *327* (3), 1335−1347.

(8) Hanson, A. B.; Nizinski, C. A.; McDonald, L. W. Effect of Diel Cycling Temperature, Relative Humidity, and Synthetic Route on the Surface Morphology and Hydrolysis of α-U3O8. *ACS Omega* **2021**, *6* (28), 18426−18433.

(9) Nizinski, C. A.; Olson, J.; Chalifoux, A. M.; Kurtyka, N.; Athon, M. T.; Tenner, T.; McDonald, L. W. Identification and Elemental Impurity Analysis of Heterogeneous Morphologies in Uranium Oxides Synthesized from Uranyl Fluoride Precursors. *ACS Omega* **2023**, *8* (19), 16896−16906.

(10) Olsen, A. M.; Richards, B.; Schwerdt, I.; Heffernan, S.; Lusk, R.; Smith, B.; Jurrus, E.; Ruggiero, C.; McDonald, L. W. Quantifying Morphological Features of α-U3O8 with Image Analysis for Nuclear Forensics. *Anal. Chem.* **2017**, *89* (5), 3177−3183.

(11) Nizinski, C. A.; Ly, C.; Vachet, C.; Hagen, A.; Tasdizen, T.; McDonald, L. W. Characterization of uncertainties and model generalizability for convolutional neural network predictions of uranium ore concentrate morphology. *Chemom. Intell. Lab. Syst.* **2022**, *225*, No. 104556.

(12) Ly, C.; Olsen, A. M.; Schwerdt, I. J.; Porter, R.; Sentz, K.; McDonald, L. W.; Tasdizen, T. A new approach for quantifying morphological features of U 3 O 8 for nuclear forensics using a deep learning model. *J. Nucl. Mater.* **2019**, *517*, 128−137.

(13) de Jonge, N.; Ross, F. M. Electron microscopy of specimens in liquid. *Nat. Nanotechnol.* **2011**, *6* (11), 695−704.

(14) de Yoreo, J. J. In-situ liquid phase TEM observations of nucleation and growth processes. *Prog. Cryst. Growth Charact. Mater.* **2016**, *62* (2), 69−88, DOI: 10.1016/j.pcrysgrow.2016.04.003.

(15) Sattonnay, G.; Ardois, C.; Corbel, C.; Lucchini, J. F.; Barthe, M.-F.; Garrido, F.; Gosset, D. Alpha-radiolysis effects on UO 2 alteration in water. *J. Nucl. Mater.* **2001**, *288*, 11 DOI: 10.1016/S0022-3115(00)00714-5.

(16) Guo, X.; Wu, D.; Xu, H.; Burns, P. C.; Navrotsky, A. Thermodynamic studies of studtite thermal decomposition pathways via amorphous intermediates UO3, U2O7, and UO4. *J. Nucl. Mater.* **2016**, *478*, 158−163.

(17) Burns, P. C.; Hughes, K.-A. Studtite,[(UO2)(O2)(H2O)2](H2O) 2: The first structure of a peroxide mineral. *Am. Mineral.* **2003**, *88* (7), 1165−1168.

(18) Lobeck, H. L.; Isner, J. K.; Burns, P. C. Lobeck, Transformation of Uranyl Peroxide Studtite, [(UO2)(O2)(H2O)2](H2O)2, to Soluble Nanoscale Cage Clusters. *Inorg. Chem.* **2019**, *58* (10), 6781−6789.

(19) Abrefah, J.; Marschman, S. C.; Jenson, E. D. *Examination of the Surface Coatings Removed from K-East Basin Fuel Elements*; Pacific Northwest National Laboratory: Richland, WA Report-11806; 1998 DOI: 10.2172/291174.

(20) McNamara, B.; Hanson, B. D.; Buck, E. C.; Soderquist, C. Corrosion of commercial spent nuclear fuel. 2. Radiochemical analyses of metastudtite and leachates. *Radiochim. Acta* **2005**, *93*, 169 DOI: 10.1524/ract.93.3.169.61615.

(21) Abbott, E. C.; O'Connor, H. E.; Nizinski, C. A.; Gibb, L. D.; Allen, E. W.; McDonald, L. W. Thermodynamic evaluation of the uranyl peroxide synthetic route on morphology. *J. Nucl. Mater.* **2022**, *561*, No. 153533.

(22) Buck, E. C.; Wittman, R. S.; Soderquist, C. Z.; McNamara, B. K. Monitoring bromide effect on radiolytic yields using in situ observations of uranyl oxide precipitation in the electron microscope. *RSC Adv.* **2018**, *8* (33), 18227−18233.

(23) Abellan, P.; Woehl, T. J.; Parent, L. R.; Browning, N. D.; Evans, J. E.; Arslan, I. Factors influencing quantitative liquid (scanning) transmission electron microscopy. *Chem. Commun.* **2014**, *50* (38), 4873−4880.

(24) Schneider, N. M.; Norton, M. M.; Mendel, B. J.; Grogan, J. M.; Ross, F. M.; Bau, H. H. Electron-Water interactions and implications for liquid cell electron microscopy. *J. Phys. Chem. C* **2014**, *118* (38), 22373−22382.

(25) Hanson, A. B.; Lee, R. N.; Vachet, C.; Schwerdt, I. J.; Tasdizen, T.; McDonald, L. W. Quantifying impurity effects on the surface morphology of α-U3O8. *Anal. Chem.* **2019**, *91* (15), 10081−10087.

(26) Karuppasamy, M.; et al. *J. Synch Radiation* **2011**, *18* (3), 398−412.

(27) Liu, L.; Kruska, K.; Hall, G. B.; Clark, R. A.; Meier, D. E.; Buck, E. C. Formation and growth of cerium (III) oxalate nanocrystals by liquid-cell transmission electron microscopy. *Scr. Mater.* **2022**, *219*, No. 114856.

(28) Woehl, T. J.; Abellan, P. Defining the radiation chemistry during liquid cell electron microscopy to enable visualization of nanomaterial growth and degradation dynamics. *J. Microsc.* **2017**, *265* (2), 135−147.

(29) Gludovatz, B.; Hohenwarter, A.; Catoor, D.; Chang, E. H.; George, E. P.; Ritchie, R. O. A fracture-resistant high-entropy alloy for cryogenic applications. *Science* **2014**, *345* (6201), 1153−1158.

(30) Demopoulos, G. P. Aqueous precipitation and crystallization for the production of particulate solids with desired properties. *Hydrometallurgy* **2009**, *96* (3), 199−214.

(31) Thanh, N. T. K.; Maclean, N.; Mahiddine, S. Mechanisms of nucleation and growth of nanoparticles in solution. *Chem. Rev.* **2014**, *114* (15), 7610−7630, DOI: 10.1021/cr400544s.

(32) Nielson, M. H.; Aloni, S.; De Yoreo, J. J. In situ TEM imaging of $CaCO_3$ nucleation reveals coexistence of direct and indirect pathways. *Science* **2014**, *345*, 1158−1162.

(33) Jin, B.; Liu, Z.; Shao, C.; Chen, J.; Liu, L.; Tang, R.; de Yoreo, J. J. Phase Transformation Mechanism of Amorphous Calcium Phosphate to Hydroxyapatite Investigated by Liquid-Cell Transmission Electron Microscopy. *Cryst. Growth Des.* **2021**, *21* (9), 5126−5134.

(34) de Yoreo, J. J.; Gilbert, P. U. P. A.; Sommerdijk, N. A. J. M.; Penn, R. L.; Whitelam, S.; Joester, D.; Zhang, H.; Rimer, J. D.; Navrotsky, A.; Banfield, J. F.; Wallace, A. F.; Michel, F. M.; Meldrum, F. C.; Cölfen, H.; Dove, P. M. Crystallization by particle attachment in synthetic, biogenic, and geologic environments. *Science* **2015**, *349* (6247), aaa6760 DOI: 10.1126/science.aaa6760.
(35) Van Santen, R. A. The Ostwald Step Rule. *J. Phys. Chem.* **1984**, *88*, 5768 DOI: 10.1021/j150668a002.
(36) Mikhlin, Y.; Karacharov, A.; Likhatski, M.; Podlipskaya, T.; Zubavichus, Y.; Veligzhanin, A.; Zaikovski, V. Submicrometer intermediates in the citrate synthesis of gold nanoparticles: New insights into the nucleation and crystal growth mechanisms. *J. Colloid Interface Sci.* **2011**, *362* (2), 330−336.
(37) Vekilov, P. G. Dense liquid precursor for the nucleation of ordered solid phases from solution. *Cryst. Growth Des.* **2004**, *4* (4), 671−685.
(38) Vekilov, P. G. Nucleation. *Cryst. Growth Des.* **2010**, *10* (12), 5007−5019.
(39) Jehannin, M.; Rao, A.; Cölfen, H. New Horizons of Nonclassical Crystallization. *J. Am. Chem. Soc.* **2019**, *141* (26), 10120−10136, DOI: 10.1021/jacs.9b01883.
(40) Rey, A.; Utsunomiya, S.; Giménez, J.; Casas, I.; de Pablo, J.; Ewing, R. C. Stability of uranium (VI) peroxide hydrates under ionizing radiation. *Am. Mineral.* **2009**, *94* (2−3), 229−235.
(41) Baumgartner, J.; Dey, A.; Bomans, P. H.; Le Coadou, C.; Fratzl, P.; Sommerdijk, N. A.; Faivre, D. Nucleation and growth of magnetite from solution. *Nat. Mater.* **2013**, *12* (4), 310−314.
(42) Weck, P. F.; Kim, E.; Jové-Colón, C. F.; Sassani, D. C. Structures of uranyl peroxide hydrates: A first-principles study of studtite and metastudtite. *Dalton Transactions* **2012**, *41* (32), 9748−9752.
(43) Egerton, R. F.; Li, P.; Malac, M. Radiation damage in the TEM and SEM. *Micron* **2004**, *35* (6), 399−409.
(44) Kabler, M. N.; Williams, R. T. Vacancy-interstitial pair production via electron-hole recombination in halide crystals *Phys. Rev. B* **1978**, *18*, 1948−1960.
(45) Jiang, N. Electron beam damage in oxides: A review. *Rep. Prog. Phys.* **2015**, *79* (1), No. 016501, DOI: 10.1088/0034-4885/79/1/016501.
(46) Hobbs, L. W. The role of topology and geometry in the irradiation-induced amorphization of network structures. In. *J. Non-Cryst. Solids* **1995**, *182*, 27 DOI: 10.1016/0022-3093(94)00574-5.
(47) Traboulsi, A.; Vandenborre, J.; Blain, G.; Humbert, B.; Barbet, J.; Fattahi, M. Radiolytic corrosion of uranium dioxide: role of molecular species. *J. Phys. Chem. C* **2014**, *118* (2), 1071−1080.

https://doi.org/10.1021/acsomega.3c07743
ACS Omega 2023, 8, 48336−48343